

Indenter tip radius effect on the Nix–Gao relation in micro- and nanoindentation hardness experiments

S. Qu and Y. Huang^{a)}

Department of Mechanical and Industrial Engineering, University of Illinois, Urbana, Illinois 61801

W.D. Nix

Department of Material Science and Engineering, Stanford University, Stanford, California 94305

H. Jiang

Department of Mechanical and Industrial Engineering, University of Illinois, Urbana, Illinois 61801

F. Zhang and K.C. Hwang

Department of Engineering Mechanics, Tsinghua University, Beijing 100084, China

(Received 24 June 2004; accepted 20 August 2004)

Nix and Gao established an important relation between microindentation hardness and indentation depth. Such a relation has been verified by many microindentation experiments (indentation depths in the micrometer range), but it does not always hold in nanoindentation experiments (indentation depths approaching the nanometer range). We have developed a unified computational model for both micro- and nanoindentation in an effort to understand the breakdown of the Nix–Gao relation at indentation depths approaching the nanometer scale. The unified computational model for indentation accounts for various indenter shapes, including a sharp, conical indenter, a spherical indenter, and a conical indenter with a spherical tip. It is based on the conventional theory of mechanism-based strain gradient plasticity established from the Taylor dislocation model to account for the effect of geometrically necessary dislocations. The unified computational model for indentation indeed shows that the Nix–Gao relation holds in microindentation with a sharp indenter, but it does not hold in nanoindentation due to the indenter tip radius effect.

I. INTRODUCTION

Microindentation hardness experiments have repeatedly shown that the indentation hardness of crystalline materials displays a strong size effect. The measured indentation hardness of metallic materials typically increases by a factor of two or three as the indentation depth decreases to submicrons, that is, *smaller is harder*.^{1–10} Based on the Taylor dislocation model^{11,12} and a model of geometrically necessary dislocations (GND) underneath a sharp indenter tip shown in the inset of Fig. 1, Nix and Gao¹³ established the following relation between the microindentation hardness H and the indentation depth h for a *sharp, conical indenter*

$$\left(\frac{H}{H_0}\right)^2 = 1 + \frac{h^*}{h}, \quad (1)$$

where h^* is a characteristic length given by Nix and Gao¹³ that depends on not only the properties of the

indented material but also the indenter angle, and it is typically of the order micrometers, and H_0 is the indentation hardness for a large indentation depth (e.g., $h \gg h^*$). The above relation is based on the self-similar deformation field underneath the sharp indenter, and it predicts a linear relation between H^2 and $1/h$, which corresponds to a straight line in the $H^2 \sim 1/h$ plot. Figure 1 shows the microindentation hardness data for single-crystal and polycrystalline copper⁸ as well as for single-crystal silver.⁶ It is clearly observed that the *microindentation hardness* for a *sharp, conical indenter* agrees very well with the Nix–Gao relation (1) over the entire range of indentation depth above 0.2 μm .

There are, however, some recent *nanoindentation hardness* data for a *sharp, conical indenter* that does not obey the Nix–Gao relation (1). As shown in Fig. 2, Lim and Chaudhri's¹⁴ nanoindentation hardness data with the Berkovich indenter for annealed copper start to deviate from the Nix–Gao relation (1) (the straight line in Fig. 2) when the indentation depth h is of the order submicrometers. Even though the indentation hardness continues to increase as the indentation depth decreases (i.e., *smaller is still harder*), the hardness data are significantly lower

^{a)}Address all correspondence to this author.

e-mail: huang9@uiuc.edu
DOI: 10.1557/JMR.2004.0441

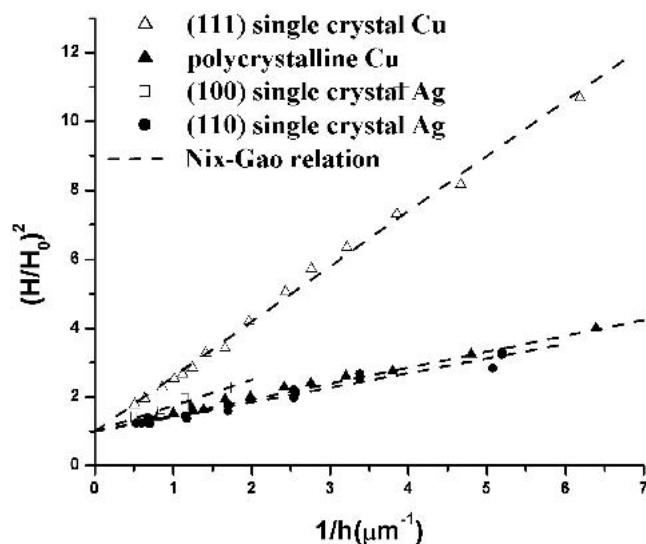


FIG. 1. Microindentation hardness data for single-crystal and polycrystalline copper,⁸ as well as for single crystal silver.⁶ Here h is the indentation depth, H is the microindentation hardness, and H_0 is the indentation hardness for large depths of indentation. The Nix–Gao relation (1) is also shown for each set of experimental data, and it agrees well with the microindentation hardness data. The inset shows Nix and Gao’s¹³ model of geometrically necessary dislocations underneath a sharp indenter.

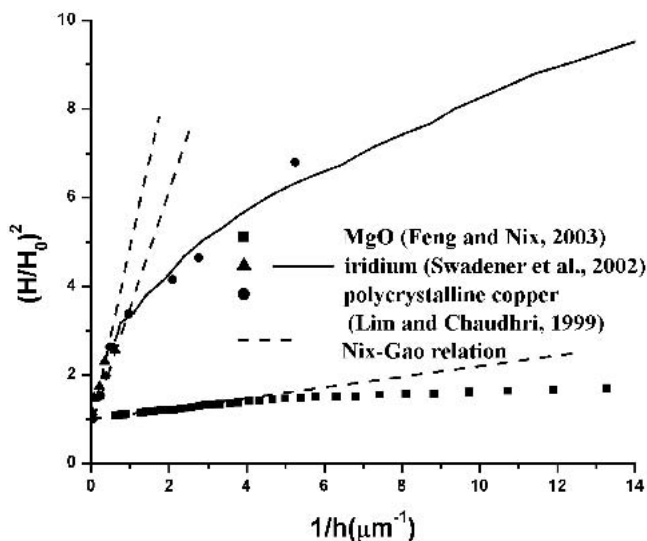


FIG. 2. Micro- and nanoindentation hardness data for annealed polycrystalline copper¹⁴, annealed iridium¹⁶, and MgO.¹⁷ The Nix–Gao relation (1) is also shown for each set of experimental data, and it does *not* agree well with the nanoindentation hardness data.

than the straight line predicted by Nix and Gao.¹³ Swadener et al.¹⁵ also used the Berkovich indenter and showed that the nanoindentation hardness data for annealed iridium are smaller than that given by the Nix–Gao relation (1) when the indentation depth h becomes submicrometer (Fig. 2). Recently, Feng and Nix¹⁶ and

Elmustafa and Stone¹⁷ found that, once the indentation depth is less than $0.2 \mu\text{m}$, the Nix–Gao relation (1) does not hold in MgO (Fig. 2) and in annealed α -brass and aluminum, respectively. It is clear that the linear relation (1) between H^2 and $1/h$ predicted by Nix and Gao¹³ does not hold in nanoindentation with the indentation depth of the order submicrometer or below. However, the cause of this deviation from the Nix–Gao relation in nanoindentation is still unclear.

Besides nanoindentation, there also exist other micro-indentation hardness data that do not follow the Nix–Gao relation (1) at micrometer-depth indentations.^{14,15,18–21} The indenters in these experiments are primarily *spherical indenters*¹⁵ or *conical indenters with spherical tips*.¹⁹ These spherical indentation data consistently show the opposite depth dependence of indentation hardness, that is, the indentation hardness decreases with the indentation depth¹⁵—*smaller is softer*. These indentation hardness data from spherical indentation experiments do not follow the Nix–Gao relation (1), which was established for a sharp, conical indenter.

The objective of this paper is to study a possible cause of the deviation of nanoindentation hardness from the Nix–Gao relation (1). We adopt a single, unified computational model for both micro- and nanoindentation with different indenter shapes, including (i) a “sharp”, conical indenter; (ii) a spherical indenter; and (iii) a conical indenter with a spherical tip.

Similar to Nix and Gao,¹³ our analysis is based on the Taylor dislocation model.^{11,12} However, the GND density for a conical indenter with a spherical tip cannot be simply estimated as Nix and Gao¹³ did for a sharp, conical indenter because the deformation field underneath the spherical indenter tip is no longer self-similar. We adopt the conventional theory of mechanism-based strain gradient plasticity (CMSG),²² which is also established from the Taylor dislocation model^{11,12} and can account for nonuniform distributions of GND density underneath a spherical indenter tip. We use the finite element method for CMSG to study the indentation hardness and to predict the distribution of dislocation density underneath the indenter.

The outline of this paper is as follows. Section II gives a summary of CMSG, and Sec. III provides details of the unified computational model for both micro- and nanoindentation with different indenter shapes, including a sharp, conical indenter, a spherical indenter, and a conical indenter with a spherical tip. The numerical results in Sec. IV based on the unified computational model for indentation indeed show that, due to the indenter tip radius effect, the microindentation hardness (indentation depth above submicrometer) agrees well with the Nix–Gao relation (1), but nanoindentation hardness (indentation depth on the order of submicrometer or below) does not obey the Nix–Gao relation. (Here the indenter tip

radius effect refers to the change of indenter tip geometry from a sharp tip to a round tip).

II. TAYLOR DISLOCATION MODEL AND THE CONVENTIONAL THEORY OF MECHANISM-BASED STRAIN GRADIENT PLASTICITY

A. Taylor dislocation model

The shear flow stress τ is related to the dislocation density ρ by^{11,12,23}

$$\tau = \alpha\mu b \sqrt{\rho} \quad , \quad (2)$$

where μ is the shear modulus, b is the magnitude of Burgers vector, and α is an empirical coefficient around 0.3. The dislocation density ρ is composed of the density ρ_S for statistically stored dislocations (SSD), which accumulate by trapping each other in a random way,²⁴ and the density ρ_G for geometrically necessary dislocations (GND), which are required for compatible deformation of various parts of the nonuniformly deformed material,^{24–26} that is,

$$\rho = \rho_S + \rho_G \quad . \quad (3)$$

The GND density ρ_G is related to the curvature of plastic deformation,^{13,24} or effective plastic strain gradient η^p , by

$$\rho_G = \bar{r} \frac{\eta^p}{b} \quad , \quad (4)$$

where \bar{r} is the Nye factor introduced by Arsenlis and Parks²⁷ to reflect the effect of crystallography on the distribution of GNDs, and \bar{r} is around 1.90 for face-centered-cubic (fcc) polycrystals.^{27,28}

The tensile flow stress σ_{flow} is related to the shear flow stress τ by

$$\sigma_{flow} = M\tau \quad , \quad (5)$$

where M is the Taylor factor which acts as an isotropic interpretation of the crystalline anisotropy at the continuum level, and $M = 3.06$ for fcc metals^{29–31} as well as for body-centered-cubic bcc metals that slip on {110} planes.³¹ The substitution of (2)–(4) into (5) yields

$$\sigma_{flow} = M\alpha\mu b \sqrt{\rho_S + \bar{r} \frac{\eta^p}{b}} \quad . \quad (6)$$

For uniaxial tension, the flow stress can also be related to the plastic strain ϵ^p by $\sigma_{flow} = \sigma_{ref}f(\epsilon^p)$, where σ_{ref} is a reference stress and f is a nondimensional function determined from the uniaxial stress–strain curve. Because the plastic strain gradient η^p vanishes in uniaxial tension, the SSD density ρ_S is determined from Eq. (6) as

$\rho_S = [\sigma_{ref}f(\epsilon^p)/(M\alpha\mu b)]^2$.¹³ The flow stress in Eq. (6) then becomes

$$\begin{aligned} \sigma_{flow} &= \sqrt{[\sigma_{ref}f(\epsilon^p)]^2 + M^2\bar{r}\alpha^2\mu^2b\eta^p} \\ &= \sigma_{ref}\sqrt{f^2(\epsilon^p) + l\eta^p} \quad , \end{aligned} \quad (7)$$

where

$$l = M^2\bar{r}\alpha^2\left(\frac{\mu}{\sigma_{ref}}\right)^2 b = 18\alpha^2\left(\frac{\mu}{\sigma_{ref}}\right)^2 b \quad , \quad (8)$$

is the intrinsic material length in strain gradient plasticity, $M = 3.06$ and $\bar{r} = 1.90$. This intrinsic material length represents a natural combination of the effects of elasticity (via the shear modulus μ), plasticity (via the reference stress σ_{ref}) and atomic spacing (via the Burgers vector b). It is important to note that, even though this intrinsic material length l depends on the choice of the reference stress σ_{ref} in uniaxial tension, the flow stress σ_{flow} in Eq. (7) *does not* because the strain gradient term inside the square root in Eq. (7) becomes $\sigma_{ref}^2l\eta^p = 18\alpha^2\mu^2b\eta^p$ and is independent of σ_{ref} .

B. An alternative expression of the uniaxial stress–strain curve

Huang et al.²² suggested to rewrite the uniaxial stress–plastic strain relation $\sigma = \sigma_{ref}f(\epsilon^p)$ to the following viscoplastic expression^{32–34} to pave the way for the establishment of CMSG

$$\dot{\epsilon}^p = \dot{\epsilon}_0 \left[\frac{\sigma}{\sigma_{ref}f(\epsilon^p)} \right]^m \quad , \quad (9)$$

where $\dot{\epsilon}^p$ is the rate of plastic strain, $\dot{\epsilon}_0$ is a reference strain rate, and m is the rate-sensitivity exponent which usually takes a large value ($m \geq 20$). In the limit $m \rightarrow \infty$, Eq. (9) degenerates to $\sigma = \sigma_{ref}f(\epsilon^p)$. Equation (9), however, displays a strain-rate sensitivity such that the resulting stress–strain relation depends on the normalized time $\dot{\epsilon}_0 t$, even though this rate sensitivity is rather weak for a large m (≥ 20).

Following Kok et al.,^{35–37} Huang et al.²² proposed to replace the reference strain rate $\dot{\epsilon}_0$ by the effective strain rate $\dot{\epsilon}$ to eliminate the strain-rate sensitivity. Equation (9) then becomes

$$\dot{\epsilon}^p = \dot{\epsilon} \left[\frac{\sigma}{\sigma_{ref}f(\epsilon^p)} \right]^m \quad . \quad (10)$$

In the limit $m \rightarrow \infty$, Eq. (10) also degenerates to the uniaxial stress–strain relation $\sigma = \sigma_{ref}f(\epsilon^p)$. Because Eq. (10) has strain rate on both sides, *the resulting stress–strain relation becomes independent of the strain rate*, that is, the strains do not change once the stresses are fixed. Figure 3 shows the uniaxial stress–strain relation for rate sensitivity exponent $m = 5, 20$, and ∞ obtained by Huang et al.²² All modeling parameters can be found in Huang et al.²² It is clearly observed that all curves are

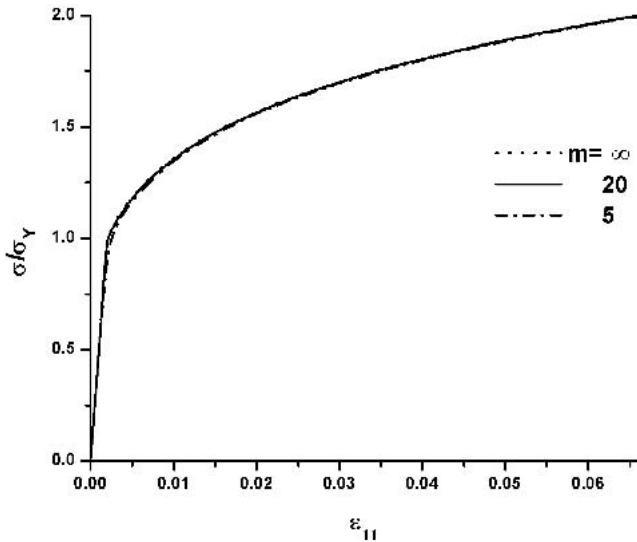


FIG. 3. Uniaxial stress–strain relation for rate sensitivity exponent $m = 5, 20,$ and ∞ ; σ_Y is the initial yield stress; plastic work hardening exponent $N = 0.2$, the ratio of yield stress to Young’s modulus $\sigma_Y/E = 0.2\%$, Poisson’s ratio $\nu = 0.3$. The limit $m = \infty$ corresponds to the conventional power-law hardening relation $\sigma = \sigma_Y(1 + CE\epsilon^P/\sigma_Y)^N$.

very close, and there is essentially no difference between the curves for $m = 20$ and $m = \infty$. Therefore, Eq. (10) with $m \geq 20$ is an excellent representation of the uniaxial stress–strain relation $\sigma = \sigma_{ref}f(\epsilon^P)$. Even though such an approach looks complex, it paves the way to establish CMSG based on the Taylor dislocation model, as discussed in the following.

C. The constitutive model in CMSG

The volumetric strain rate $\dot{\epsilon}_{kk}$ and deviatoric strain rate $\dot{\epsilon}'_{ij}$ in CMSG plasticity are related to the stress rate in the same way as in classical plasticity, that is,

$$\dot{\epsilon}_{kk} = \frac{\dot{\sigma}_{kk}}{3K} \quad , \quad (11)$$

$$\dot{\epsilon}'_{ij} = \dot{\epsilon}'_{ij}{}^e + \dot{\epsilon}'_{ij}{}^p = \frac{\dot{\sigma}'_{ij}}{2\mu} + \frac{3\dot{\epsilon}^P}{2\sigma_3} \sigma'_{ij} \quad , \quad (12)$$

where K and μ are the elastic bulk and shear moduli, $\dot{\epsilon}'_{ij}{}^e$ and $\dot{\epsilon}'_{ij}{}^p$ are the elastic deviatoric and plastic strain rates, respectively, σ'_{ij} is the deviatoric stress, and $\sigma_e = (3\sigma'_{ij}\sigma'_{ij}/2)^{1/2}$ is the effective stress. The effective plastic strain rate $\dot{\epsilon}^P = (2\dot{\epsilon}'_{ij}\dot{\epsilon}'_{ij}/3)^{1/2}$ is obtained from Eq. (10) except that the tensile flow stress $\sigma_{ref}f(\epsilon^P)$ in the denominator is replaced by the flow stress in Eq. (7) established from the Taylor dislocation model accounting for the strain gradient effect, that is,

$$\dot{\epsilon}^P = \dot{\epsilon} \left(\frac{\sigma_e}{\sigma_{flow}} \right) = \dot{\epsilon} \left[\frac{\sigma_e}{\sigma_{ref}\sqrt{f^2(\epsilon^P) + l\eta^P}} \right]^m \quad , \quad (13)$$

where $\dot{\epsilon} = (2\dot{\epsilon}'_{ij}\dot{\epsilon}'_{ij}/3)^{1/2}$. Equations (11)–(13) can be rearranged to give the stress rate in terms of the strain rate,

$$\dot{\sigma}_{ij} = K\dot{\epsilon}_{kk}\delta_{ij} + 2\mu \left\{ \dot{\epsilon}'_{ij} - \frac{3\dot{\epsilon}}{2\sigma_e} \left[\frac{\sigma_e}{\sigma_{ref}\sqrt{f^2(\epsilon^P) + l\eta^P}} \right]^m \sigma'_{ij} \right\} \quad . \quad (14)$$

This is the constitutive relation in CMSG, which involves the conventional stress and strain only. The plastic strain gradient comes into play to reduce the incremental plastic modulus, similar to Acharya and Bassani³⁸ and Acharya and Beaudoin.³⁹ CMSG also bears similarity with Evers et al.⁴⁰ viscoplastic strain gradient plasticity theory because CMSG would have been viscoplastic if $\dot{\epsilon}_0$ were not replaced by $\dot{\epsilon}$ in Eq. (10). Furthermore, Huang et al.²² compared CMSG with the higher order theory of mechanism-based strain gradient plasticity (MSG)^{41–43} that is also established from the Taylor dislocation model.^{11,12} Figure 4 shows the strain distributions given by CMSG and the higher order theory of MSG for a bar subject to a constant body force to illustrate their differences. All modeling parameters can be found in Huang et al.²² It is clearly observed that CMSG and MSG give the same strain distribution except within thin boundary layers near the two ends. These boundary layers are due to the additional boundary conditions introduced in the higher-order theory of MSG. Furthermore, Shi et al.⁴⁴ showed that the thickness of boundary layers

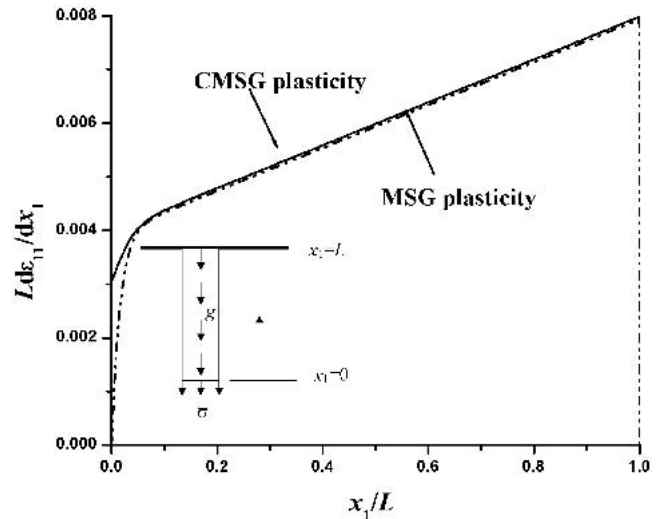


FIG. 4. The distribution of strain gradient $Ld\epsilon_{11}/dx_1$ in the bar predicted by CMSG (solid line) and MSG plasticity (dashed curve) theories for bar length $L = 0.1l$, where l is the intrinsic material length in strain gradient plasticity. The material parameters are the plastic work hardening exponent $N = 0.5$, Poisson’s ratio $\nu = 0.5$, the ratio of yield stress to Young’s modulus $\sigma_Y/E = 0.2\%$, and rate sensitivity exponent $m = 20$.

is on the order of L^2/l , and is typically around 10 nm for metallic materials, where L is the average dislocation spacing and l is the intrinsic material length in Eq. (8). Therefore, CMSG can characterize the deformation of solids to the same accuracy as the higher order theory of MSG except in the thin boundary layers whose thickness is on the order of 10 nm.

The effective plastic strain gradient η^p in CMSG is defined in the same way as that in the higher-order MSG theory,^{41–43} and is given by

$$\begin{aligned} \eta^p &= \int \dot{\eta}^p dt, \quad \dot{\eta}^p = \sqrt{\frac{1}{4} \dot{\eta}_{ijk}^p \dot{\eta}_{ijk}^p}, \\ &= \dot{\epsilon}_{ik,j}^p + \dot{\epsilon}_{jk,i}^p - \dot{\epsilon}_{ij,k}^p, \end{aligned} \quad (15)$$

where $\dot{\epsilon}_{ij}^p$ is the tensor of plastic strain rate.

The equilibrium equations in CMSG are identical to those in conventional continuum theories. There are no extra boundary conditions beyond those in conventional continuum theories. Therefore, CMSG is simpler than the higher-order strain gradient plasticity theories, though it may not be accurate within thin boundary layers of the solid.

D. Finite element analysis for CMSG

Unlike the higher order theories of strain gradient plasticity,^{41–43,45–48} CMSG does not involve the higher order stress such that the equilibrium equations, kinematic relations between strain and displacement, and boundary conditions are identical to those in classical plasticity theories. Only the constitutive model is modified to account for the plastic strain gradient effect. Therefore, CMSG does not require new finite elements (while the aforementioned higher order theories do), and the use of only conventional finite elements makes it easy and straightforward to implement CMSG in the finite element program. In fact, we have implemented CMSG in the ABAQUS finite element program⁴⁹ via its USER-MATERIAL subroutine UMAT.⁵⁰ The only effort beyond that in classical plasticity is the evaluation of plastic strain gradient within UMAT, which is accomplished numerically by interpolating the plastic strain increment $\Delta \epsilon^p$ within each element via the values at Gaussian integration points in the isoparametric space, and by determining the gradient of plastic strain increment via the differentiation of the shape function.

Besides simplicity, another advantage of CMSG in the indentation analysis based on the ABAQUS is that only the USER-MATERIAL subroutine UMAT is needed. This allows the rigorous modeling of contact between the indented material and indenter. On the contrary, the higher-order theories of strain gradient plasticity^{43,51–53} require the USER-ELEMENT subroutine UEL (for new elements), which cannot be combined with any contact

models in ABAQUS, and require additional assumptions and iterative procedures in the indentation analysis, as further discussed in the next section.

III. A UNIFIED COMPUTATIONAL MODEL FOR BOTH MICRO- AND NANOINDENTATION WITH VARIOUS INDENTERS

The indentation hardness is defined in the usual way as the mean pressure exerted by the indenter at the maximum load. In this section, we develop a unified computational model for both micro- and nanoindentation with three different indenter shapes. Here micro- and nanoindentation refer to indentation depth above and below submicrometers, respectively.

Figure 5 shows a schematic diagram of (i) a sharp, conical indenter with the cone angle of 140.6° ; (ii) a spherical indenter with radius R ; and (iii) a conical indenter with a spherical tip of radius R .

Here the cone angle is 140.6° (Fig. 5) such that the conical indenter gives the same contact area $A = 24.5h^2$ as the Berkovich indenter at the same indentation depth h .¹² For simplicity, the indenter is assumed to be rigid and axisymmetric, which is a standard assumption in all existing indentation models based on strain gradient plasticity.^{43,51–54} For the conical indenter with a spherical tip, there exists a critical contact radius $a_c = R \cos 70.3^\circ = 0.34R$ which separates the spherical and conical indentation (Fig. 5). For contact radius $a < a_c$, the conical part of the indenter is not in contact with the indented material such that the indentation is the same as that for a spherical indenter of the same radius. For $a \gg a_c$, the conical indenter with a spherical tip becomes essentially the same as the sharp, conical indenter because the effect of indenter tip becomes negligible.

Indentation can be represented by the contact model between the rigid indenter and the indented material in the finite element analysis. The finite sliding, hard contact model in ABAQUS⁴⁹ is used, which allows the sliding between two contact surfaces but no interpenetration.

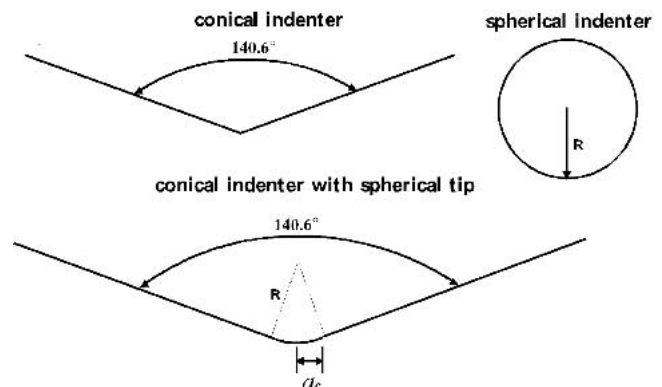


FIG. 5. Schematic diagrams of a sharp, conical indenter with the cone angle of 140.6° ; a spherical indenter with radius R ; and a conical indenter (cone angle 140.6°) with a spherical tip of radius R .

The normal and shear tractions are continuous within the contact zone, and they vanish outside the contact zone. We have studied both frictionless contact (i.e., vanishing shear stress tractions) and frictional contact (i.e., the shear stress traction related to normal stress traction via the friction coefficient). For the friction coefficient less than or equal to 0.2, there are essentially no differences between the indentation hardness predicted by the frictional and frictionless contact models. Only the results for frictionless contact are presented in the following.

The contact model has the advantage that the contact radius, which is needed to determine the contact area and therefore the indentation hardness, can be determined directly from the finite element analysis. The contact model can be used together with UMAT, but not with the USER-ELEMENT subroutine UEL in ABAQUS. The higher order theories of strain gradient plasticity, which usually involve UEL, must involve additional approximations to determine the contact radius and indentation hardness. For example, Begley and Hutchinson,⁵¹ Huang et al.,⁴³ and Xue et al.⁵² imposed only the displacement normal to the surface of the indented material and neglected displacements tangential to the surface. Furthermore, they used an iterative, time-consuming procedure to determine the contact radius. The current analysis based on CMSG avoids these additional approximations and iterations.

IV. MICRO- AND NANOINDENTATION HARDNESS

In this section, we use the unified computational model for indentation in Sec. III to study the micro- and nanoindentation hardness of annealed copper⁸ and provide an explanation for the Nix–Gao relation (1) to hold in microindentation but not in nanoindentation hardness experiments. For annealed copper, McElhaney et al.⁸ and Nix and Gao¹³ reported the indentation hardness $H_0 = 834$ MPa for large indentation depths (\gg micrometers, no strain gradient effect).

A. Material properties of annealed copper

The relation between flow stress σ_{flow} and plastic strain ϵ^p in uniaxial tension can be generally expressed via the power law as

$$\sigma_{\text{flow}} = \sigma_{\text{ref}} f(\epsilon^p) = \sigma_Y \left(1 + C \frac{E \epsilon^p}{\sigma_Y} \right)^N, \quad (16)$$

where σ_Y is the yield stress in uniaxial tension, E is the Young's modulus, N (< 1) is the plastic work hardening exponent, and C is a dimensionless parameter to be determined from the uniaxial stress–strain curve and is of the order 1. For the limit of vanishing plastic strain $\epsilon^p \rightarrow 0$, the flow stress degenerates to the yield stress σ_Y . In the other limit of plastic strain much larger than the yield

strain σ_Y/E , the flow stress σ_{flow} becomes proportional to $(\epsilon^p)^N$, that is, a power law. The reference stress in Eq. (16) can be taken as $\sigma_{\text{ref}} = \sigma_Y (E/\sigma_Y)^N$, and the function f then becomes $f(\epsilon^p) = (\sigma_Y/E + C\epsilon^p)^N$.

The Young's modulus $E = 109$ GPa for copper and Poisson's ratio $\nu = 0.3$ give the shear modulus $\mu = 42$ GPa, which agrees with the value reported by McElhaney et al.⁸ The Burgers vector is $b = 0.255$ nm. We take the plastic work hardening exponent $N = 0.3$ for annealed polycrystalline copper, which agrees with the experimental data.^{43,55,56} The yield stress for annealed copper is taken as $\sigma_Y = 76.8$ MPa^{52,57} such that the indentation hardness for large indentation depths (\gg micrometers, no strain gradient effect) agrees with the experimental value $H_0 = 834$ MPa reported by McElhaney et al.⁸ and Nix and Gao.¹³ The rate sensitivity exponent is $m = 20$, and $C = 0.73$.

B. Microindentation hardness for a sharp, conical indenter

Another parameter that remains to be determined is the coefficient α in the Taylor dislocation model in (2). This coefficient α appears in the intrinsic material length l in Eq. (8) and therefore influences the depth-dependent micro- and nanoindentation hardness. Nix and Gao¹³ determined α from the depth-dependent hardness of annealed copper in microindentation (i.e., indentation depth above submicrometer). Their model was for a sharp indenter because the SEM micrographs of McElhaney et al.⁸ microindentation experiments showed that, over the scale of $1 \mu\text{m}$, the indenter tip was still very sharp such that the tip radius must be about $0.1 \mu\text{m}$ or less. In fact, Nix and co-workers have estimated the indenter tip radius by measuring the elastic contact (with displacement up to 10 nm) on flat fused quartz and observed a Hertz-type force–displacement relation from which the tip radius can be determined. It is confirmed that the radius of sharp indenter is indeed about $0.1 \mu\text{m}$ or less. Therefore, the sharp, conical model can be used for microindentation experiments whose depth of indentation is larger than submicrometer.

We also use the model of sharp, conical indenter, together with the computational model for indentation in Sec. III and CMSG, to determine the coefficient α from McElhaney and colleagues'⁸ microindentation hardness data for annealed polycrystalline copper. The cone angle is 140.6° (Fig. 5). Only the microindentation data for the indentation depth above $0.3 \mu\text{m}$ are used to ensure that the effect of indenter tip radius ($< 0.1 \mu\text{m}$) can be neglected such that the sharp indenter model holds. Figure 6 shows the microindentation hardness $[(H/H_0)^2]$ predicted by CMSG versus the reciprocal of indentation depth ($1/h$) for polycrystalline copper, where $H_0 = 834$ MPa is the indentation hardness for large depth of indentation (\gg micrometers) given by Nix and Gao.¹

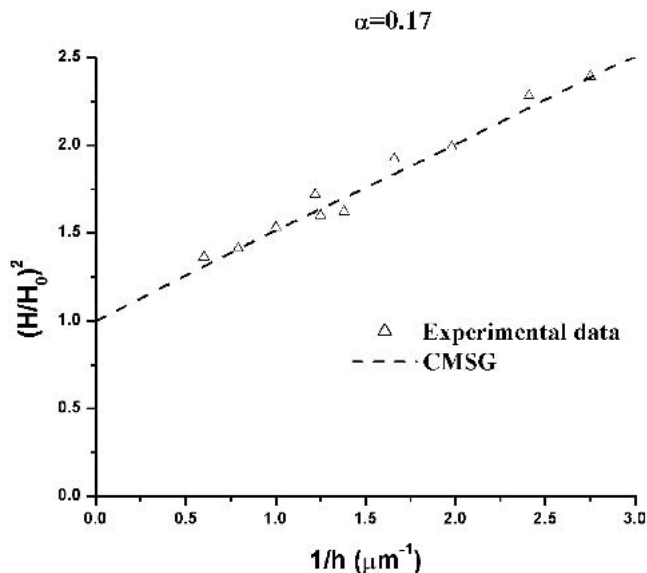


FIG. 6. The depth dependence of indentation hardness for polycrystalline copper. Here H is the microindentation hardness, H_0 is the hardness for large depths of indentation, and h is the indentation depth. The material properties are Young's modulus $E = 109$ GPa, Poisson's ratio $\nu = 0.3$, plastic work hardening exponent $N = 0.3$, yield stress $\sigma_y = 76.8$ MPa, Burgers vector $b = 0.255$ nm, rate sensitivity exponent $m = 20$, and the coefficient in the Taylor dislocation model $\alpha = 0.17$. The experimental data of McElhane et al.⁸ have been replotted by Nix and Gao.¹³

The coefficient α in the Taylor dislocation model is taken as 0.17. The experimental data of McElhane et al.⁸ for annealed copper are also shown in Fig. 6 for comparison. It is observed that the microindentation hardness predicted by CMSG agrees very well with the experimentally measured indentation hardness for indentation depth larger than $0.3 \mu\text{m}$. Moreover, the numerical results

based on CMSG do give a straight line in Fig. 6, and agree with the Nix–Gao relation (1). This confirms that the Nix–Gao relation (1) holds in microindentation with a sharp indenter.

To explain why the Nix–Gao relation (1) holds in microindentation, we show the contour plots of statistically stored dislocation (SSD) density ρ_S and geometrically necessary dislocation (GND) density ρ_G in Figs. 7, 8, and 9. Here we use $\rho_S = [\sigma_{ref} f(\epsilon^p)/(M\alpha\mu b)]^2$ in Sec. II and $\rho_G = \bar{r}\gamma^p/b$ in (4) to obtain the SSD and GND densities from the plastic strain and strain gradient, respectively. The indentation depths are $h = 2 \mu\text{m}$ and $0.067 \mu\text{m}$, where $h = 0.067 \mu\text{m}$ is already in the nanoindentation range. Each contour is shown for a region of $31.3h \times 19.6h$ underneath the indenter, and the region scales with the indentation depth h . It is observed that the distribution of SSD density for a relatively large indentation depth $h = 2 \mu\text{m}$ in Fig. 7(a) is almost identical to that for a much smaller indentation depth $h = 0.067 \mu\text{m}$ in Fig. 7(b). This suggests that the distribution of SSD density for a sharp indenter is self similar, and takes the form

$$\rho_S = \frac{1}{bl} \tilde{\rho}_S \left(\frac{x}{h}, \frac{y}{h}, \frac{z}{h} \right), \quad (17)$$

where b is the Burgers vector, l is the intrinsic material length in Eq. (8), and $\tilde{\rho}_S$ is a nondimensional function of position normalized by the indentation depth h .

Figure 8 shows the contour plots of GND density ρ_G for the same indentation depths. The GND density for the relatively large indentation depth $h = 2 \mu\text{m}$ is much lower than that for small indentation depth $h = 0.067 \mu\text{m}$, that is, the GND density increases as the indentation depth decreases. The Nix–Gao model¹³ suggests

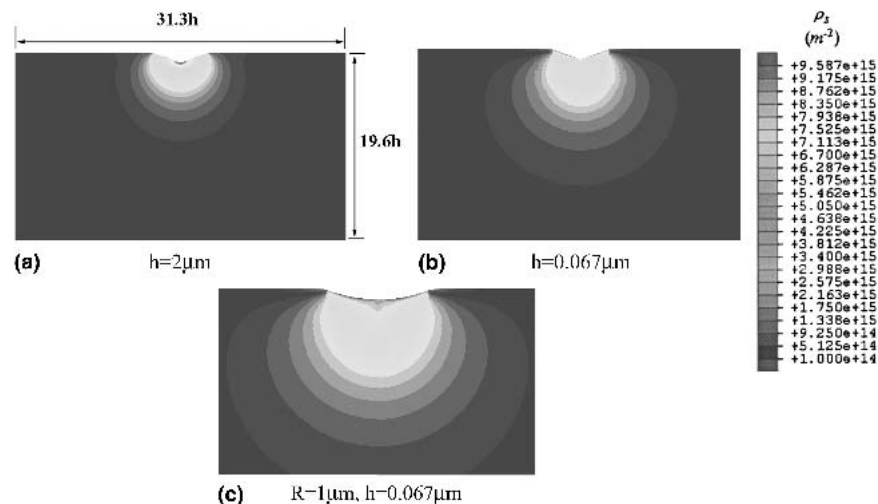


FIG. 7. Contour plots of statistically stored dislocation density in a region of $31.3h \times 19.6h$ underneath the indenter, where h is the indentation depth. (a) A sharp, conical indenter (cone angle 140.6°) at $h = 2 \mu\text{m}$; (b) a sharp conical indenter (cone angle 140.6°) at $h = 0.067 \mu\text{m}$; and (c) a conical indenter (cone angle 140.6°) with spherical tip (tip radius $R = 1 \mu\text{m}$) at $h = 0.067 \mu\text{m}$. The contours range from $10^{14}/\text{m}^2$ to $10^{16}/\text{m}^2$. The material properties are the same as those in Fig. 6.

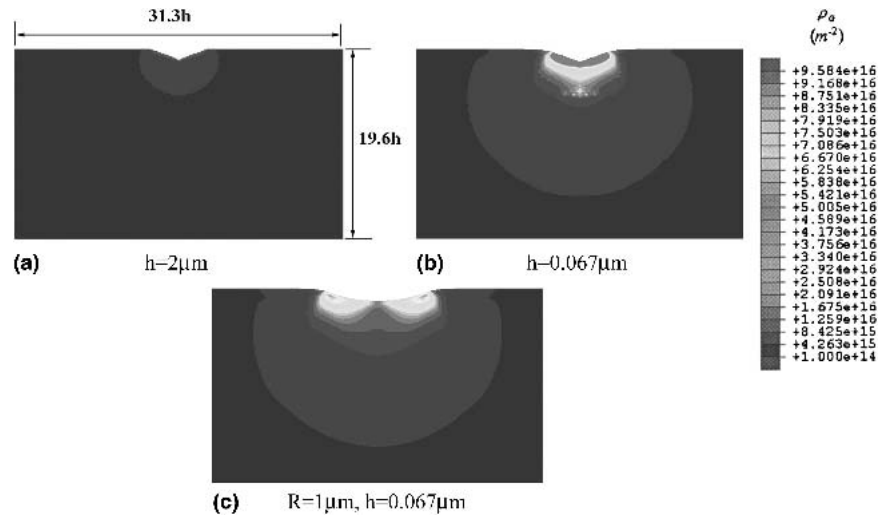


FIG. 8. Contour plots of geometrically necessary dislocation density in a region of $31.3h \times 19.6h$ underneath the indenter, where h is the indentation depth. (a) A sharp, conical indenter (cone angle 140.6°) at $h = 2 \mu\text{m}$; (b) a sharp conical indenter (cone angle 140.6°) at $h = 0.067 \mu\text{m}$; and (c) a conical indenter (cone angle 140.6°) with spherical tip (tip radius $R = 1 \mu\text{m}$) at $h = 0.067 \mu\text{m}$. The contours range from $10^{14}/\text{m}^2$ to $10^{17}/\text{m}^2$. The material properties are the same as those in Fig. 6.

the GND density to be proportional to $1/h$. To verify this $1/h$ dependence, we show the contour plots of $\rho_G h$ in Fig. 9. It is observed that the contour plots of $\rho_G h$ are almost identical for indentation depths $h = 2 \mu\text{m}$ and $0.067 \mu\text{m}$, which confirms that $\rho_G \propto 1/h$ in the Nix–Gao model. Therefore, the GND density ρ_G takes the form

$$\rho_G = \frac{1}{bh} \tilde{\rho}_G \left(\frac{x}{h}, \frac{y}{h}, \frac{z}{h} \right), \quad (18)$$

where b is the Burgers vector, and $\tilde{\rho}_G$ is a nondimensional function of position normalized by the indentation depth h . The substitution of Eqs. (17) and (18) into the Taylor dislocation model (2) leads to the $1/h$ dependence of σ_{flow}^2 (or equivalently, H^2).

The Nix and Gao model¹³ assumes a constant GND density proportional to $1/h$ in a semisphere underneath the indenter and a vanishing GND density outside the semisphere. On the contrary, Fig. 8 shows continuous distributions of GND density that is not constant and decays away from the indenter tip. In fact, the comparison of Figs. 7 and 8 indicates that the GND density decays much faster than the SSD density away from the indenter tip. Therefore, the effect of GND is very localized around the indenter such that the assumption of vanishing GND density outside a semisphere in the Nix–Gao model¹³ is not unreasonable. It is interesting to note from Fig. 8 that the contours of constant GND density are approximately semispheres, which provides

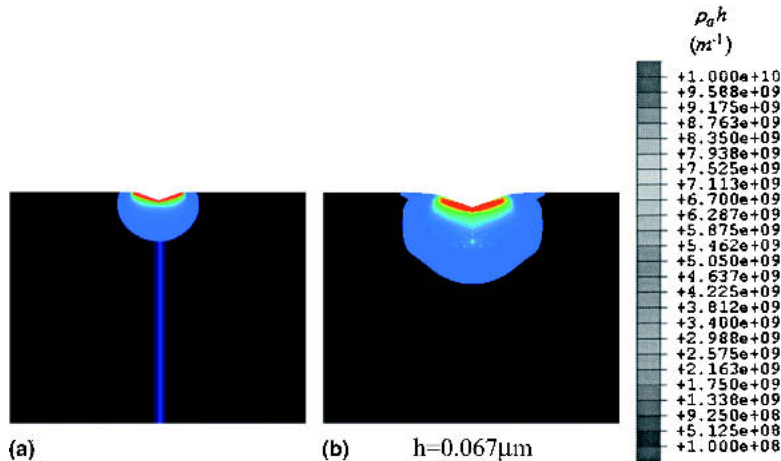


FIG. 9. Contour plots of $\rho_G h$ for the same two indentation depths (a) $h = 2 \mu\text{m}$ and (b) $0.067 \mu\text{m}$ as in Figs. 7 and 8 for a sharp, conical indenter. Here, ρ_G is geometrically dislocation density. The material properties are the same as those in Fig. 6. The region is $31.3h \times 19.6h$ underneath the indenter.

the validation for the assumption of GND in a hemisphere in the Nix–Gao model.¹³

The good agreement between the experimentally measured and numerically predicted microindentation hardness in Fig. 6 provides the validation of CMSG theory and the computational model for indentation in Sec. III. We use such a model in the next section to study the indenter tip radius effect in microindentation.

C. Microindentation hardness for a conical indenter with a spherical tip

We use the unified computational model for indentation in Sec. III to investigate the effect of indenter tip radius in microindentation of a conical indenter with a spherical tip. All material properties are given in Sec. IV. A, and the coefficient α in the Taylor dislocation model is $\alpha = 0.17$ (Sec. IV. B). The cone angle is 140.6° (Fig. 5), and the radius of spherical tip is $R = 1 \mu\text{m}$. Figure 10 shows the microindentation hardness versus the contact radius a predicted by CMSG for a conical indenter with a spherical tip. The contact radius a is related to the indentation depth via the geometry of the indenter. The results for a sharp, conical indenter with the same cone angle (140.6°) and for a spherical indenter with the same radius ($1 \mu\text{m}$) are also presented in Fig. 10 for comparison. The minimal contact radius a presented in Fig. 10 is about $0.2 \mu\text{m}$, at which the indentation depth is $h = 0.072 \mu\text{m}$ for the sharp, conical indenter, and $h = 0.02 \mu\text{m}$ for the spherical indenter and for the conical indenter with a spherical tip. The sharp, conical indenter gives monotonically increasing indentation hardness

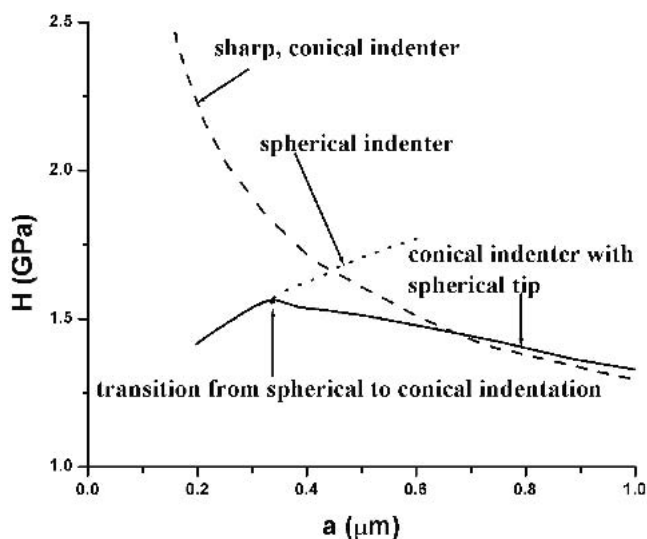


FIG. 10. Microindentation hardness versus the contact radius predicted by CMSG for a conical indenter with a spherical tip; a sharp, conical indenter with the same cone angle (140.6°); and a spherical indenter with the same radius ($R = 1 \mu\text{m}$). The material properties are the same as those in Fig. 6.

with the decreasing indentation depth, which is consistent with the experimental observations “smaller is harder” for a sharp indenter. For the spherical indenter, the indentation hardness displays the opposite depth dependence, that is, the indentation hardness decreases with the indentation depth, which agrees with the experiments with spherical indenter.^{14,15} Xue et al.⁵² developed a simple model to explain this opposite depth dependence for sharp and spherical indenters. They showed that, for a sharp indenter, the average plastic strain underneath the indenter is essentially independent of the indentation depth (i.e., self-similar deformation field), but the plastic strain gradient is proportional to $1/h$. For a spherical indenter, however, the plastic strain gradient becomes independent of h , but the average plastic strain increases with the indentation contact radius. These observations, together with the Taylor dislocation model (2), lead to the opposite depth dependence of indentation hardness for sharp and spherical indenters.

For a conical indenter with a spherical tip, the indentation hardness is the same as that for a spherical indenter when the contact radius a is less than the critical contact radius $a_c = 0.34R$. For $a > a_c$, the conical part of the indenter is in contact with the indented material; the corresponding curve in Fig. 10 for the conical indenter with a spherical tip deviates from that for the spherical indenter. The critical point separating spherical and conical indentation is marked in Fig. 10. As the indentation depth continues to increase, the curve for the conical indenter with a spherical tip gradually approaches that for the sharp, conical indenter, as the effect of indenter tip radius gradually diminishes. This point will become clearer in Fig. 11 to be shown later.

One important observation from Fig. 10 is that, contrary to the sharp, conical indenter and spherical indenter, the indentation hardness for the conical indenter with a spherical tip does not display a monotonic dependence on the contact radius in microindentation. As shown in Fig. 10, the indentation hardness (i) initially increases with the contact radius a (due to the strain hardening associated with spherical contact); (ii) reaches a peak value; and (iii) then decreases with the contact radius a (due to strain gradient effect).

This non-monotonic depth dependence of indentation hardness may explain some opposite experimental observations for a conical indenter with a spherical tip. For example, as the indentation depth increases, Swadener et al.¹⁵ observed the increase of indentation hardness in spherical indentation, whereas Tyimiak et al.¹⁹ observed the opposite for a conical indenter with a spherical tip. This difference may be because the indentation data of Tyimiak et al.¹⁹ are on the descending part of the curve for a conical indenter with a spherical tip in Fig. 10.

Figures 7(c) and 8(c) show the SSD and GND densities for a conical indenter (cone angle 140.6°) with

spherical tip (tip radius $R = 1 \mu\text{m}$), respectively. All material properties are the same as in previous sections. The indentation depth is $h = 0.067 \mu\text{m}$, which is also the same as the smaller indentation depth in previous sections. It is important to point out that the contact radius at this indentation depth $h = 0.067 \mu\text{m}$ is $a = 0.36 \mu\text{m}$, which is slightly larger than the critical contact radius $a_c = 0.34R$ ($R = 1 \mu\text{m}$) such that the indentation has finished the spherical part and just reaches the conical part. It is interesting to observe from Figs. 7(c) and 7(b) that the SSD densities at $h = 0.067 \mu\text{m}$ are very close for conical indenters with spherical tip and sharp tip. This means that, soon after the conical part of the indenter is reached, the tip radius has little effect on the SSD density. On the contrary, the GND density in Fig. 8(c) for a conical indenter with a spherical tip is much smaller than that in Fig. 8(b) for a sharp tip. This is not surprising, because the sharp tip leads to large strain concentration and therefore large strain gradient and GND density.

We show the indentation hardness in the plot of $(H/H_0)^2$ versus $1/h$ in Fig. 11 for a conical indenter with a spherical tip, a sharp, conical indenter with the same cone angle (140.6°), and a spherical indenter with the same radius ($R = 1 \mu\text{m}$). The curve for the conical indenter with a spherical tip coincides with that for the spherical indenter at small indentation depth (large $1/h$). It gradually approaches the curve for the sharp, conical indenter at large indentation depth (small $1/h$), and eventually approaches H_0 at very large indentation depths. The range of $1/h$ in Fig. 11 is much larger than that in Fig. 6 and is clearly in the nanoindentation range (smallest indentation depth $\sim 50 \text{ nm}$). The sharp, conical indenter always gives a straight line in the $(H/H_0)^2 \sim 1/h$ plot, including in

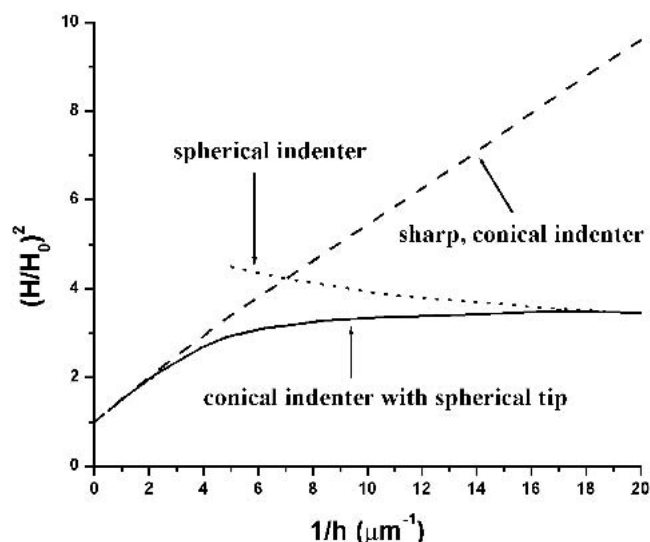


FIG. 11. The plot of $(H/H_0)^2$ versus $1/h$ for a conical indenter with a spherical tip, a sharp conical indenter with the same cone angle (140.6°), and a spherical indenter with the same tip radius ($R = 1 \mu\text{m}$). The material properties are the same as those in Fig. 6.

nanoindentation. This suggests that, without accounting for the effect of indenter tip radius, CMSG cannot explain why the nanoindentation hardness obtained in experiments does not follow the Nix–Gao relation (1).

D. Nanoindentation hardness

The indentation depth h is below submicrometer in nanoindentation. For such small h , the indenter tip radius effect must be accounted for, even for a “sharp” indenter whose indenter tip radius is of the order $0.1 \mu\text{m}$ or less, as such tip radius may be larger than the indentation depth in nanoindentation.

We have used the unified model of conical indenter with a spherical tip of radius R in Sec. III to study the nanoindentation hardness. All material properties (including the coefficient α in the Taylor dislocation model) are the same as those in Sec. IV. A and Sec. IV. B. The cone angle is 140.6° , and the radius of the spherical tip R ranges from 0 to $1 \mu\text{m}$, where $R = 0$ corresponds to an idealized model of atomistically sharp tip in the Nix–Gao model.¹³ Figure 12 shows $(H/H_0)^2$ versus $1/h$ for tip radius $R = 0, 0.1, 0.2,$ and $1 \mu\text{m}$. Here $1/h$ ranges up to 30, corresponding to the indentation depth around 30 nm. The microindentation hardness data of McElhane et al.⁸ for annealed polycrystalline copper are also shown in Fig. 12 for comparison. The curves for tip radius $R \leq 0.2 \mu\text{m}$ agree well with the experimental data because the indenter tip radius effect is negligible in microindentation (for a “sharp” indenter as in the experiments of McElhane et al.⁸ experiments). However, once the indentation depth is less than about $0.13 \mu\text{m}$, the curves start to separate and deviate from the straight line

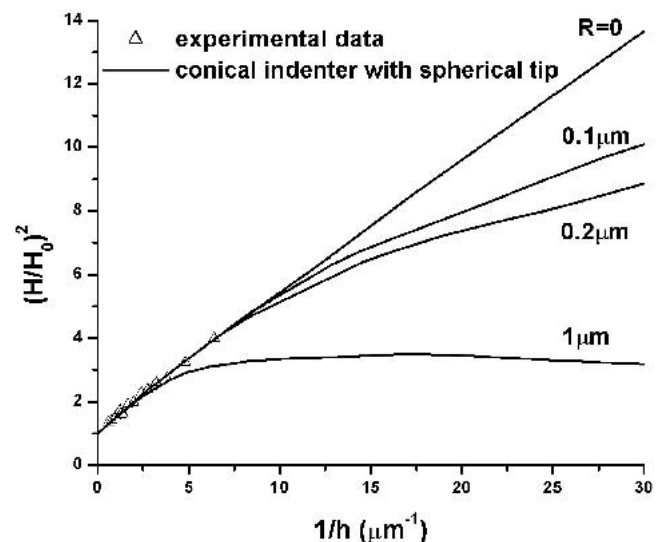


FIG. 12. The plot of $(H/H_0)^2$ versus $1/h$ for a conical indenter with a spherical tip, and tip radius $R = 0, 0.1, 0.2,$ and $1 \mu\text{m}$. The material properties are the same as those in Fig. 6. The experimental data of McElhane et al.⁸ are also shown.

for $R = 0$ (the Nix–Gao relation). For example, at the small indentation depth around 30 nm, the values of $(H/H_0)^2$ for $R = 0.1 \mu\text{m}$ and $0.2 \mu\text{m}$ are only 73.0% and 64.7% of that for $R = 0$, respectively, and are significantly smaller than the Nix–Gao relation (1) (the straight line in Fig. 10). This shows that, due to the indenter tip radius effect, the nanoindentation hardness may deviate from the Nix–Gao relation (1). In other words, the indenter tip radius may be partially responsible for the deviation of nanoindentation hardness from the Nix–Gao relation (1). The indenter tip radius effect becomes more drastic for tip radius $R = 1 \mu\text{m}$, whose curve is much lower and even decreases with the indentation depth (increasing $1/h$).

It is noted that the deviation of nanoindentation hardness from the Nix–Gao relation (1) predicted by CMSG for polycrystalline copper in Fig. 12 is less than the experimental deviation for other materials reported in Fig. 2. This suggests that this deviation may depend strongly on materials and the tip radius of the indenter used in experiments. There may also be other mechanisms that contribute to the deviation.¹⁶

V. CONCLUSIONS

We have developed a unified computational model for both micro- and nanoindentation to study the Nix–Gao relation (1) between indentation hardness and indentation depth. The unified computational model for indentation accounts for various indenter shapes, including a sharp, conical indenter, a spherical indenter, and a conical indenter with a spherical tip. It is based on the conventional theory of mechanism-based strain gradient plasticity² established from the Taylor dislocation model^{11,12} to account for the effect of geometrically necessary dislocations. The unified computational model for indentation shows that the Nix–Gao relation holds in microindentation with sharp indenter, but it does not hold in nanoindentation due to the indenter tip radius effect.

ACKNOWLEDGMENTS

Y.H. acknowledges support from NSF (Grant No. CMS-0084980) and ONR (Grant No. N00014-01-1-0205, program officer Dr. Y.D.S. Rajapakse). Support from NSFC is also acknowledged. Y.H. and W.D.N. gratefully acknowledge support from an NSF-NIRT project “Mechanism Based Modeling and Simulation in Nanomechanics,” through Grant No. NSF CMS-0103257, under the direction of Dr. Ken Chong.

REFERENCES

- W.D. Nix: Mechanical properties of thin films. *Mater. Trans.* **20A**, 2217 (1989).
- W.C. Oliver and G.M. Pharr: An improved technique for determining hardness and elastic modulus using loading and displacement sensing indentation. *J. Mater. Res.* **7**, 1564 (1992).
- M.S. de Guzman, G. Neubauer, P.A. Filinn, and W.D. Nix: The role of indentation depth on the measured hardness of materials, in *Thin Films: Stresses and Mechanical Properties IV*, edited by P.H. Townsend, T.P. Weihs, J.E. Sanchez, Jr., and P. Borgensen (Mater. Res. Soc. Symp. Proc. **308**, Pittsburgh, PA, 1993) p. 613.
- N.A. Stelmashenko, A.G. Walls, L.M. Brown, and Y.V. Milman: Microindentation on W and Mo oriented single crystals: An STM study. *Acta Metall. Mater.* **41**, 2855 (1993).
- M. Atkinson: Further analysis of the size effect in indentation hardness tests of some metals. *J. Mater. Res.* **10**, 2908 (1995).
- Q. Ma and D.R. Clarke: Size dependent hardness of silver single crystals. *J. Mater. Res.* **10**, 853 (1995).
- W.J. Poole, M.F. Ashby, and N.A. Fleck: Micro-hardness of annealed and work-hardened copper polycrystals. *Scripta Mater.* **34**, 559 (1996).
- K.W. McElhaney, J.J. Vlassak, and W.D. Nix: Determination of indenter tip geometry and indentation contact area for depth-sensing indentation experiments. *J. Mater. Res.* **13**, 1300 (1998).
- S. Suresh, T.G. Nieh, and B.W. Choi: Nano-indentation of copper thin films on silicon substrates. *Scripta Mater.* **41**, 951 (1999).
- A.V. Zagrebelny, E.T. Lilleodden, W.W. Gerberich, and C.B. Carter: Indentation of silicate-glass films on Al_2O_3 substrates. *J. Am. Ceram. Soc.* **82**, 1803 (1999).
- G.I. Taylor: The mechanism of plastic deformation of crystals. Part I.—theoretical. *Proc. R. Soc. London A.* **145**, 362 (1934).
- G.I. Taylor: Plastic strain in metals. *J. Inst. Metals* **62**, 307 (1938).
- W.D. Nix and H. Gao: Indentation size effects in crystalline materials: a law for strain gradient plasticity. *J. Mech. Phys. Solids* **46**, 411 (1998).
- Y.Y. Lim and M.M. Chaudhri: The effect of the indenter load on the nanohardness of ductile metals: An experimental study on polycrystalline work-hardened and annealed oxygen-free copper. *Philos. Mag. A* **79**, 2879 (1999).
- J.G. Swadener, E.P. George, and G.M. Pharr: The correlation of the indentation size effect measured with indenters of various shapes. *J. Mech. Phys. Solids* **50**, 681 (2002).
- G. Feng and W.D. Nix: Indentation size effect in MgO. *Scripta Mater.* **51**, 599 (2004).
- A.A. Elmestafa and D.S. Stone: Nanoindentation and the indentation size effect: Kinetics of deformation and strain gradient plasticity. *J. Mech. Phys. Solids* **51**, 357 (2003).
- Y.Y. Lim, A.J. Bushby, and M.M. Chaudhri: Nano and macro indentation studies of polycrystalline copper using spherical indenters, in *Fundamentals of Nanoindentation and Nanotribology*, edited by N.R. Moody, W.W. Gerberich, N. Burnham, and S.P. Baker (Mater. Res. Soc. Symp. Proc. **522**, Warrendale, PA, 1998) p. 145.
- N.I. Tymiak, D.E. Kramer, D.F. Bahr, T.J. Wyrobek, and W.W. Gerberich: Plastic strain and strain gradients at very small indentation depths. *Acta Mater.* **49**, 1021 (2001).
- N. Iwashita and M.V. Swain: Elasto-plastic deformation of silica glass and glassy carbons with different indenters. *Philos. Mag. A* **82**, 2199 (2002).
- S.O. Kucheyev, J.E. Bradby, J.S. Williams, and C. Jagadish: Mechanical deformation of single-crystal ZnO. *Appl. Phys. Lett.* **80**, 956 (2002).
- Y. Huang, S. Qu, K.C. Hwang, M. Li, and H. Gao: A conventional theory of mechanism-based strain gradient plasticity. *Int. J. Plast.* **20**, 753 (2004).
- J.E. Bailey and P.B. Hirsch: The dislocation distribution, flow stress, and stored energy in cold-worked polycrystalline silver. *Philos. Mag.* **5**, 485 (1960).

24. M.F. Ashby: The deformation of plastically non-homogeneous alloys. *Philos. Mag.* **21**, 399 (1970).
25. J.F. Nye: Some geometrical relations in dislocated crystals. *Acta Metall. Mater.* **1**, 153 (1953).
26. A.H. Cottrell: *The Mechanical Properties of Materials* (J. Wiley, New York, 1964), p. 277.
27. A. Arsenlis and D.M. Parks: Crystallographic aspects of geometrically-necessary and statistically-stored dislocation density. *Acta Mater.* **47**, 1597 (1999).
28. M. Shi, Y. Huang, and H. Gao: The J-integral and geometrically necessary dislocations in nonuniform plastic deformation. *Int. J. Plast.* **20**, 1739 (2004).
29. J.F.W. Bishop and R. Hill: A theory of plastic distortion of a polycrystalline aggregate under combined stresses. *Philos. Mag.* **42**, 414 (1951).
30. J.F.W. Bishop and R. Hill: A theoretical derivation of the plastic properties of a polycrystalline face-centered metal. *Philos. Mag.* **42**, 1298 (1951).
31. U.F. Kocks: The relation between polycrystal deformation and single crystal deformation. *Metall. Mater. Trans.* **1**, 1121 (1970).
32. J.W. Hutchinson: Bounds and self-consistent estimates for creep of polycrystalline materials. *Proc. R. Soc. London A* **348**, 101 (1976).
33. G.R. Canova and U.F. Kocks: In *Seventh International Conference on Textures of Materials*, edited by C.M. Brakman, P. Jongenburger, and E.J. Mittemeijer (Soc. Mater. Sci., The Netherlands, 1984), p. 573.
34. R.J. Asaro and A. Needleman: Texture development and strain hardening in rate dependent polycrystals. *Acta Metal. Mater.* **33**, 923 (1985).
35. S. Kok, A.J. Beaudoin, and D.A. Tortorelli: A polycrystal plasticity model based on the mechanical threshold. *Int. J. Plast.* **18**, 715 (2002).
36. S. Kok, A.J. Beaudoin, and D.A. Tortorelli: On the development of stage IV hardening using a model based on the mechanical threshold. *Acta Mater.* **50**, 1653 (2002).
37. S. Kok, A.J. Beaudoin, D.A. Tortorelli, and M. Lebyodkin: A finite element model for the Portevin-Le Chatelier effect based on polycrystal plasticity. *Modell. Simul. Mater. Sci. Eng.* **10**, 745 (2002).
38. A. Acharya and J.L. Bassani: Lattice incompatibility and a gradient theory of crystal plasticity. *J. Mech. Phys. Solids* **48**, 1565 (2000).
39. A. Acharya and A.J. Beaudoin: Grain-size effect in viscoplastic polycrystals at moderate strains. *J. Mech. Phys. Solids* **48**, 2213 (2000).
40. L.P. Evers, D.M. Parks, W.A.M. Brekelmans, and M.G.D. Geers: Crystal plasticity model with enhanced hardening by geometrically necessary dislocation accumulation. *J. Mech. Phys. Solids* **50**, 2403 (2002).
41. H. Gao, Y. Huang, W.D. Nix, and J.W. Hutchinson: Mechanism-based strain gradient plasticity—I. Theory. *J. Mech. Phys. Solids* **47**, 1239 (1999).
42. Y. Huang, H. Gao, W.D. Nix, and J.W. Hutchinson: Mechanism-based strain gradient plasticity—II. Analysis. *J. Mech. Phys. Solids* **48**, 99 (2000).
43. Y. Huang, Z. Xue, H. Gao, W.D. Nix, and Z.C. Xia: A study of microindentation hardness tests by mechanism-based strain gradient plasticity. *J. Mater. Res.* **15**, 1786 (2000).
44. M. Shi, Y. Huang, H. Jiang, K.C. Hwang, and M. Li: The boundary-layer effect on the crack tip field in mechanism-based strain gradient plasticity. *Int. J. Fracture* **112**, 23 (2001).
45. N.A. Fleck and J.W. Hutchinson: A phenomenological theory for strain gradient effects in plasticity. *J. Mech. Phys. Solids* **41**, 1825 (1993).
46. N.A. Fleck and J.W. Hutchinson: In *Advances in Applied Mechanics* 33, edited by J.W. Hutchinson and T.Y. Wu (Academic Press, New York, 1997), p. 295.
47. N.A. Fleck and J.W. Hutchinson: A reformulation of strain gradient plasticity. *J. Mech. Phys. Solids* **49**, 2245 (2001).
48. M.E. Gurtin: A gradient theory of single-crystal viscoplasticity that accounts for geometrically necessary dislocations. *J. Mech. Phys. Solids* **50**, 5 (2002).
49. Hibbit, Karlsson & Sorenson, Inc.: ABAQUS/Standard user's manual version 6.2. (2001).
50. S. Qu, Y. Huang, H. Jiang, C. Liu, P.D. Wu, and K.C. Hwang: Fracture analysis in the conventional theory of mechanism-based strain gradient (CMSG) plasticity. *Int. J. Fracture* (2004) (in press).
51. M.R. Begley and J.W. Hutchinson: The mechanics of size-dependent indentation. *J. Mech. Phys. Solids* **46**, 2049 (1998).
52. Z. Xue, Y. Huang, K.C. Hwang, and M. Li: The influence of indenter tip radius on the micro-indentation hardness. *J. Eng. Mater. Technol.* **124**, 371 (2002).
53. Y. Wei and J.W. Hutchinson: Hardness trends in micron scale indentation. *J. Mech. Phys. Solids* **51**, 2037 (2003).
54. J.Y. Shu and N.A. Fleck: Strain gradient crystal plasticity: Size-dependent deformation of bicrystals. *J. Mech. Phys. Solids* **47**, 297 (1999).
55. D. McLean: *Mechanical Properties of Metals* (John Wiley & Sons, New York, 1962).
56. N.A. Fleck, G.M. Muller, M.F. Ashby, and J.W. Hutchinson: Strain gradient plasticity: Theory and experiments. *Acta Metall. Mater.* **42**, 475 (1994).
57. X. Qiu, Y. Huang, Y. Wei, H. Gao, and K.C. Hwang: The flow theory of mechanism-based strain gradient plasticity. *Mech. Mater.* **35**, 245 (2003).